CHINESE OPTICS LETTERS

Vol. 19, No. 6 | June 2021

Directly generating vortex beams in the second harmonic by a spirally structured fundamental wave

Jun Li (李 俊)[1*], Haigang Liu (刘海港)[2**], Yan Li (李 妍)[1], Xianping Wang (王贤平)[3], Minghuang Sang (桑明煌)[3], and Xianfeng Chen (陈险峰)[2,4]

[1] School of Science and Technology, Jiangxi Normal University, Nanchang 330022, China

[2] State Key Laboratory of Advanced Optical Communication Systems and Networks, School of Physics and Astronomy, Shanghai Jiao Tong University, Shanghai 200240, China

[3] Jiangxi Key Laboratory of Photoelectronics and Telecommunication, Department of Physics, Jiangxi Normal University, Nanchang 330022, China

[4] Collaborative Innovation Center of Light Manipulations and Applications, Shandong Normal University, Jinan 250358, China

*Corresponding author: junlee@jxnu.edu.cn

**Corresponding author: liuhaigang@sjtu.edu.cn

Received January 7, 2021 | Accepted February 26, 2021 | Posted Online March 30, 2021

Based on nonlinear wave mixing, we experimentally propose a scheme for directly generating optical orbital angular momentum (OAM) by a spirally structured fundamental wave interacting with a nonlinear medium, in which the nonlinear susceptibilities are homogenous. In the experiment, the second-harmonic generation of a fundamental wave carrying positive (negative) integers and fractional OAM states was investigated. This study presents a convenient approach for dynamic control of OAM of vortex beams, which may feature their applications in optical manipulation and optical communication.

Keywords: vortex beams; optical orbital angular momentum; spirally structured fundamental wave.

DOI: 10.3788/COL202119.060005

1. Introduction

It is well known in optics that circularly polarized photons carry angular momentum of $\pm\hbar$, and this is called spin angular momentum, which was firstly, to the best of our knowledge, reported by Beth in 1935[1]. Also, linearly polarized waves with a helical phase distribution $e^{il\phi}$ can carry orbital angular momentum (OAM) of $l\hbar$ per photon, where l and ϕ denote the topological charge (TC) and azimuth angle, respectively. The vortex beams carrying OAM exhibiting a donut-like-shaped intensity pattern with no limits on TC have been extensively applied in optical communication[2–5] since the TC is considered a newly additional degree of freedom to boost the capacity of optical communication. Besides, optical OAM has also been investigated in many other fields, such as optical tweezers[6–8] and quantum computation[9]. In the field of optical trapping, the OAM of vortex beams provides the torque to rotate the particles with different angular velocities. Meanwhile, quantum computation and imaging[10] have been accomplished by investigating the entanglement of OAM. These great applications are strongly dependent on the OAM generators. The continually changing phase with polar angles requires the OAM generators to have sufficient phase modulation capacity and smooth phase modulation. Such devices and components include spiral phase plates[11], holographic fork gratings[12,13], q plates[14], ring gratings[15], and liquid droplets[16]. Recently, researches on optical vortex generation have been broadened into the field of nonlinear optics. The nonlinear processes enable the generation of vortex beams to obtain at new frequencies. Nonlinear generation of vortex beams based on mechanisms for second-harmonic (SH)[17–19], third-harmonic (TH)[20], and even high-harmonic (HH)[21–24] has been investigated. In general, two efficient categories contribute to achieving new frequencies. One is to engineer the structure of nonlinear photonic crystals (NPCs), in which the second-order susceptibility $\chi^{(2)}$ is spatially modulated. The other is to functionalize the facet of the output of nonlinear crystals, which makes the beam spatial shaping and nonlinear generation available at the same time. However, the corresponding deficiencies in the above two schemes, including complex fabrications and unchangeable output beam patterns, restrict their performance on the manipulation of spatial shaping of nonlinear polarized waves. To solve these problems, the concept of a structured fundamental wave (FW), in which the wave front phase of the FW was modulated by a spatial light modulator (SLM), had been introduced into the frequency conversion in our previous studies[25–27]. The spatial structure of the FW is

modulated before its incidence into the $\chi^{(2)}$ medium to control the spatial property of the SH radiations.

In this paper, we demonstrate experimentally a simple and efficient method to generate an OAM beam in SH by utilizing an FW beam with spirally modulated phase incident into a homogenous medium. In the experiments, the phase profile of the FW carrying positive and negative integers or fractional OAM is investigated. This study reveals that the radii of ring-shaped SH vortex beams become larger with the increase of the absolute value of the TC of the structured FW. Nevertheless, the circular intensity pattern of the SH vortex beam transforms to elliptical and tilts into the opposite direction when the positive fractional TC is turned to negative. Moreover, the elliptical patterns of SH vortex beams are stretched along a certain direction by adding the absolute value of the TC of the structured FW.

2. Methods

Supposing that the light beam propagates along the z axis, a Gaussian beam is reflected by an SLM, and thus the phase information is imprinted into the input beam, so the structured FW can be rewritten as the following:

$$E_1 = A_1(x)\exp[-i(k_1 z - \omega t)] \cdot \exp[i(\pi|\vec{r}|^2)/\Lambda + il_1\varphi], \quad (1)$$

where $A_1(x) = A_1\exp(-x^2/\omega_0^2)$, in which A_1, k_1, and ω_0 represent the amplitude, wave vector, and beam width of the structured FW beam, respectively. The exponential expression $\exp[i(\pi|\vec{r}|^2)/\Lambda + il_1\varphi]$ denotes the spiral phase term, where $\vec{r} = x\vec{i} + y\vec{j}$, and l_1 and Λ are the TC and modulation period of the structured FW, respectively. Moreover, $\varphi = \arctan(ay/x)$ is the azimuthal angle, where a is the obliquity factor. Under the assumption of paraxial and undepleted pump approximation, the following equation is to describe the SH vortex beam:

$$\frac{dA_2}{dz} = \varepsilon_0\chi^{(2)}A_1^2(x) \cdot \exp[i(k_{2z} - 2k_1)z] \cdot \exp[2i(\pi|\vec{r}|^2/\Lambda)]\exp(2il_1\varphi). \quad (2)$$

The SH radiation can be highly efficiently generated under the condition of $k_{2z} - 2k_1 = 0$. The rightmost exponential term stands for the OAM of SH radiation. In our experiment, the structured FW propagates along the birefringent phase-matching direction for satisfying the momentum conservation between the wave vectors of the SH and the FW. Therefore, Eq. (2) can be simplified to the following:

$$A_2 = \varepsilon_0\chi^{(2)}A_1^2(x) \cdot L \cdot \exp[2i(\pi|\vec{r}|^2/\Lambda)]\exp(2il_1\varphi), \quad (3)$$

where L is the thickness of the homogenous nonlinear medium. From Eq. (3), we can see that the SH vortex light field is achieved by the modulated FW rather than the desired crystal. Moreover, the TC of the generated SH wave is twice that of the FW, $l_2 = 2l_1$, where l_2 is the TC of the SH wave.

3. Results and Discussion

In the experiment depicted in Fig. 1, a Gaussian beam is delivered from a mode-locked Nd:$Y_3Al_5O_{12}$ (Nd:YAG) nanosecond laser with the wavelength of 1064 nm.The duration of the output pulse is approximately 3 ns, and the repetition rate is 20 Hz. A half-wave plate (HWP) and a Glan–Taylor (G–T) prism are used to control the intensity and polarization of the Gaussian beam. After being expanded and collimated, the Gaussian beam is modulated and structured by an SLM. The SLM used in our experiment has a resolution of 512 × 512 pixels. The Gaussian beam whose beam waist is approximately 500 μm is imaged by a 4-f system to imprint the structured FW to a homogenous 5% (mole fraction) MgO:$LiNbO_3$ crystal (10 mm × 10 mm× 0.5 mm in $x \times y \times z$ dimensions) along the birefringent phase-matching direction. According to the Sellmeier equation, the angle between the propagation direction (z axis) and optic axis of the crystal is 75°. A shortpass filter is placed behind the nonlinear medium to obstruct the FW. Finally, the SH beam pattern carrying OAM is projected on a screen that is far away from the medium 12 cm and is captured by a camera.

To manifest the relationship between the generated SH vortex beams and the structured FW beams, we firstly imprint the structured FW beams with fan-like phase profiles onto the nonlinear crystal. The phase profiles of the structured FWs are plotted in Figs. 2(a1)–2(a6), in which the phase value is modulated in the range of 0 to 2π, and the modulated period Λ in Eq. (1) is chosen as 91.4 μm. As shown in Figs. 2(a1)–2(a3), the cycle index that phase swept from 0 to 2π is the same as the number of integral TC l_1 of the phase masks. Nevertheless, as shown in Figs. 2(a4)–2(a6), phase-drifting occurs when the TC is a non-integer. The second row in Fig. 2 represents the simulated SH patterns based on Eq. (3), which are close to the experimentally generated SH vortex patterns, as shown in the third row in Fig. 2. When the TC of the structured FW beam is varied from one integer ($l_1 = 1, 2, 3$) to another one ($l_1 = 3$), it is obvious that the intensity profiles shown in Figs. 2(b1)–2(b3) have a

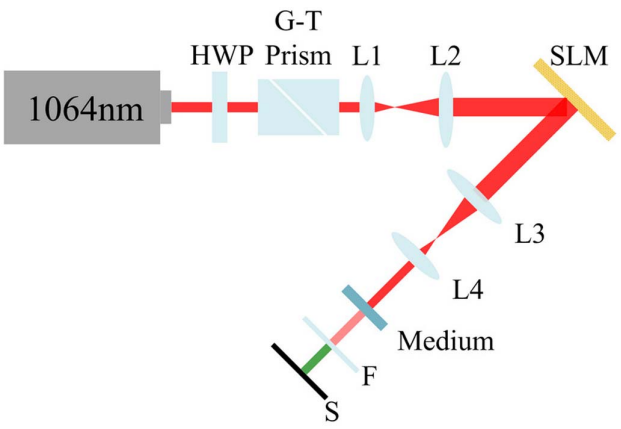

Fig. 1. Schematic of the experimental setup. HWP, half-wave plate; G-T prism, Glan–Taylor prism; L1–L4, lens with the focal length of 50, 100, 200, and 50 mm, respectively; medium, 5% (mole fraction) magnesium-oxide-doped periodically poled lithium niobate (MgO:PPLN); F, filter; S, screen.

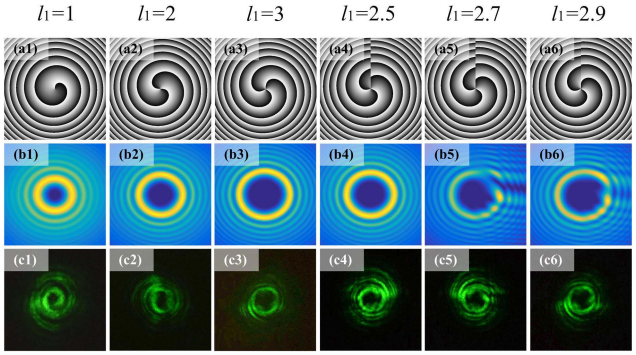

Fig. 2. Generation of the SH vortex patterns carrying different l_2, where $l_2 = 2l_1$, and l_1 is the TC of the structured FW. The first row is the phase masks of the FW beams with different TCs for (a1) $l_1 = 1$, (a2) $l_1 = 2$, (a3) $l_1 = 3$, (a4) $l_1 = 2.5$, (a5) $l_1 = 2.7$, and (a6) $l_1 = 2.9$, respectively. The second and third rows show the corresponding simulation and experimental intensity profiles of the SH vortex with different TCs for (c1) $l_2 = 2$, (c2) $l_2 = 4$, (c3) $l_2 = 6$, (c4) $l_2 = 5$, (c5) $l_2 = 5.4$, and (c6) $l_2 = 5.8$, respectively. In this case, the obliquity factor is constant ($a = 1$).

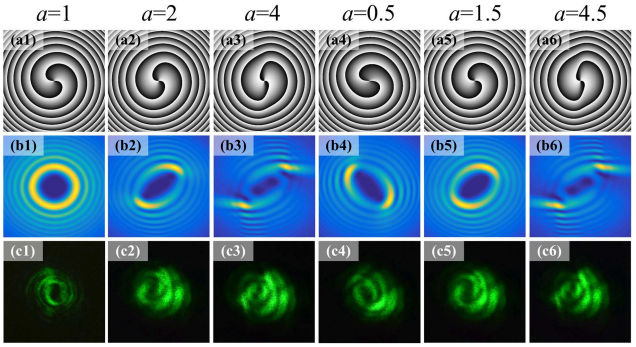

Fig. 3. Intensity patterns of the SH vortices with different obliquity factors. The first row denotes the phase profiles of the FW beams with different obliquity factors for (a1) $a = 1$, (a2) $a = 2$, (a3) $a = 4$, (a4) $a = 0.5$, (a5) $a = 1.5$, and (a6) $a = 4.5$, respectively. The TC $l_1 = 2$ is fixed in this case. The simulation and experimental intensity patterns of the SH wave are arranged and displayed in the second and the third rows, respectively.

rotationally symmetric multiple-ring structure with a dark core at the center. The diameter of dark cores increases with the increase of the TC, and the corresponding SH intensity patterns are shown in Figs. 2(c1)–2(c3). Furthermore, despite the TC of the FW beam shown in Fig. 2(a4) being fractional ($l_1 = 2.5$), a rotationally symmetric multiple-ring pattern with a dark core at the center is still observed from Fig. 2(c4). Because the TC of the SH vortex beam is an integer, the value of OAM is exactly twice that of the input FW beam ($l_2 = 2l_1 = 5$). As the TC of FW beam further increases to $l_1 = 2.7$, the first high-intensity ring shown in Fig. 2(b5) breakes into three brighter spots in a relatively darker background, and the second high-intensity ring is also visibly distorted. For $l_1 = 2.9$, the brighter spot originally formed in the second high-intensity ring has moved inward to join the former three brighter spots in the first intensity ring. The recorded patterns shown in Figs. 2(c5) and 2(c6) verify the variation of intensity distribution and agree with the simulation. It is confirmed that the intensity profiles of the SH vortices with integer TC keep a rotationally symmetric multiple-ring structure, whereas fractional TC can break and disorganize such symmetric structures to asymmetric ones.

We further consider the generation of ellipse vortex beams, in which the azimuthal angle changes according to $\varphi = \arctan(ay/x)$. The obliquity factor a has a strong influence on the intensity profile of the SH vortex beams. The intensity profiles of the SH vortices are transformed from circular into elliptical once obliquity factor a is not equal to one. The phase profiles of the FWs with $a = 1, 2, 4, 0.5, 1.5, 4.5$, respectively, are arrayed in the first row of Fig. 3, and the phase varies continuously from 0 to 2π. The twisted distortion is easily observed in spiral phase structures by changing of the obliquity factor a. Accompanying the increase of the obliquity factor, the covered area of twisted distortion grows up in size whether the numeric type of the obliquity factor is an integer or fraction. The simulation and experimentally generated patterns of the ellipse vortex beams are demonstrated in the second and the third rows of Fig. 3, respectively. The simulations and the experiments are in good agreement with each other. It can be seen that the rotationally symmetric multiple-ring shape of the SH vortex shown in Fig. 3(b1) is broken and transformed into ellipse when the obliquity factor is not equal to one, as shown in Figs. 3(b2)–3(b6). The inner bright symmetric ring of the SH vortex beam shown in Fig. 3(b1) splits into two separate brighter spots, and the circular shape of the dark core transforms into elliptical, as shown in Fig. 3(b2). Furthermore, the intensity profiles with high-order obliquity factors shown in Figs. 3(b3)–3(b6) are exhibited as two separate brighter spots. Meanwhile, the central dark core originating from Fig. 3(b1) evolves and degenerates into multiple discrete dark cores, with the location of dark cores keeping symmetry with respect to the central point of the light field. Interestingly, when the obliquity factors are reciprocal with each other, e.g., $a = 2$ and $a = 0.5$, corresponding to Figs. 3(b2) and 3(b4), the orientation of the alignment of dark cores in the two cases is perpendicular to each other. That is because the spiral phase gradient $\mathrm{d}\varphi/\mathrm{d}\theta = a/(\cos^2\theta + a^2\sin^2\theta)$ has a relative shift of 90 deg for both cases, which had been analyzed in Ref. [28].

To further reveal the conversion rule of OAM in the nonlinear frequency conversion process, we also explore the behaviors of the OAM conservation in the SH generation process by switching the sign of the optical OAM or the obliquity factor, as shown in Fig. 4. When changing the sign of TC of the FW beam with $a = 3$ from $l_1 = +2$ to $l_1 = -2$, the rotation of the elliptical SH patterns in Figs. 4(a) and 4(b) turns counterclockwise. The tilted orientation maintains its symmetry with respect to the vertical axis. The same performance is also observed in the cases shown in Figs. 4(c) and 4(d), in which the sign of the obliquity factor is switched from $a = +2$ to $a = -2$ with the fixed input OAM $l_1 = 1$. Due to the negative obliquity factor, as shown in Fig. 4(d), the spiral phase gradient $\mathrm{d}\varphi/\mathrm{d}\theta$ becomes negative and results in the opposite orientation of alignment of dark cores

in contrast with the case of $a = +2$ in Fig. 4(c). Besides, the SH generation processes possess the OAM conservation regardless of the sign of input OAM or obliquity factor. It is interesting that the number of the TC of SH vortices is conveniently and immediately read when the obliquity factor is unequal to one. For clarity, arrows shown in Fig. 4 mark the number and orientation of the dark cores. We can deduce the positive or negative value of TC of SH vortices upon the number and orientation of arrows. The OAM of the SH beam is twice as large as the input OAM of the structured FW.

In addition, the conversion efficiency of frequency-doubling process based on pump power carrying different OAM states and the SH signal power is analyzed and shown in Fig. 5. Obviously, the maximum conversion efficiency is 1.14% for SH generation, which is achieved without OAM imprinting. With the increase of the input OAM states, the conversion efficiency of the SH generation goes down dramatically. As shown in Fig. 5, the conversion efficiencies of 0.44%, 0.37%, and 0.35% are obtained experimentally at the OAM states $l_1 = 1, 2, 3$, respectively, which is consistent with the theoretical analysis based on the relationship between the conversion efficiency η and the fundamental power density of input FW beam P_1, $\eta \propto P_1 = \bar{P}/S$, where $\bar{P}$ and S denote the average power and the cross section of the structured FW beam, respectively. The decreased conversion efficiency is attributed to the increased cross section of the FW after the introduction of OAM. In our experiment, an input OAM state carrying a higher integer TC has a multiple-ring-shaped intensity profile with a bigger diameter, which results in a lower fundamental power density.

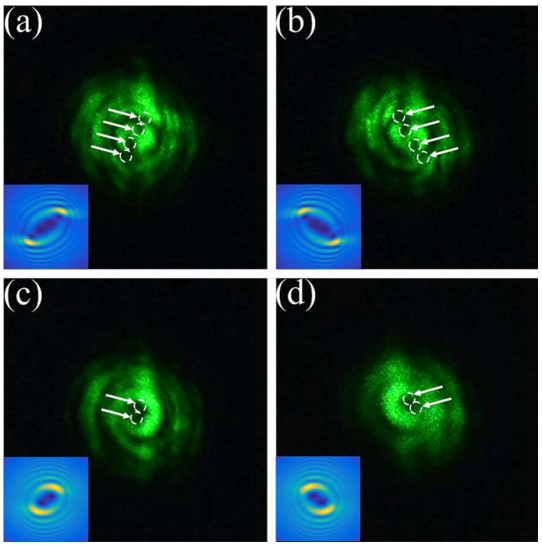

Fig. 4. Experimental comparison on the intensity patterns of generated SH waves by switching the sign of the TC of the structured FW beam and the obliquity factor, respectively. (a)–(d) Corresponding to cases of input OAM and obliquity factors that are $l_1 = +2$, $a = 3$, $l_1 = -2$, $a = 3$, $l_1 = 1$, $a = +2$, and $l_1 = 1$, $a = -2$, respectively. The insets are the corresponding simulation of SH vortex beams. The experiments are in good agreement with the simulations.

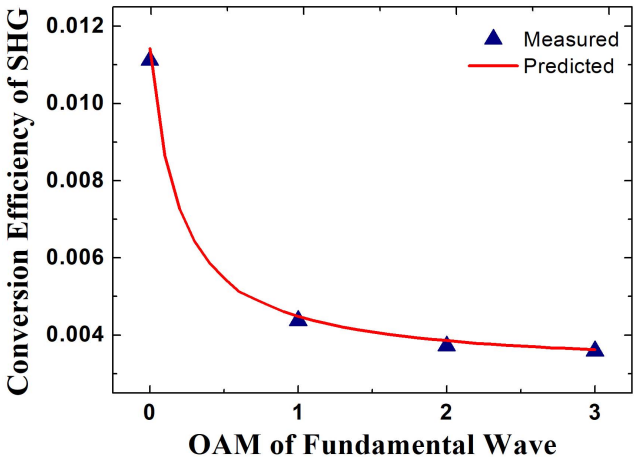

Fig. 5. Conversion efficiency of SH waves pumped by different OAM states with the fixed obliquity factor $a = 1$.

4. Conclusion

We have experimentally demonstrated the generation of vortex beams in SH by modulating the phase of the FW directly incident into a homogenous nonlinear crystal. The phase structure of the FW is dynamically controlled by an SLM, which allows us to flexibly and independently control the OAM state of the generated SH beams. In our experiments, both circular and elliptical vortex beams were investigated, and the universal conservation rule of OAM in the SH generation process was verified directly as the obliquity factor does not equal one. Our approach can generate any demanded SH signals with arbitrary OAM, which may be useful in OAM-related physical branches such as quantum optics, micromanipulation in particles, and nonlinear optics.

Acknowledgement

This work was supported by the National Natural Science Foundation of China (Nos. 11864017, 61765008, and 12064017), the Scientific and Technology Project of Jiangxi Provincial Education Department (No. GJJ161539), the Open Project of Key Laboratory of Photoelectronics and Communication of Jiangxi Province (No. 2015005), the Open Project of Jiangxi Key Laboratory of Nanomaterials and Sensors (No. 2017007), the Open Fund by State Key Laboratory of Advanced Optical Communication Systems and Networks (No. 2017GZKF18), and the Young Talent Development Plan of Jiangxi Normal University 2019.

References

1. R. A. Beth, "Direct detection of the angular momentum of light," Phys. Rev. **48**, 471 (1935).
2. J. Wang, J. Y. Yang, I. M. Fazal, N. Ahmed, Y. Yan, H. Huang, Y. Ren, Y. Yue, S. Dolinar, and M. Tur, "Terabit free-space data transmission employing orbital angular momentum multiplexing," Nat. Photon. **6**, 488 (2012).

3. B. Nenad, Y. Yang, Y. Ren, T. Moshe, K. Poul, H. Hao, A. E. Willner, and R. Siddharth, "Terabit-scale orbital angular momentum mode division multiplexing in fibers," Science **340**, 1545 (2013).
4. L. Chen, R. K. Singh, A. Dogariu, Z. Chen, and J. Pu, "Estimating topological charge of propagating vortex from single-shot non-imaged speckle," Chin. Opt. Lett. **19**, 022603 (2021).
5. Y. Liu, X. Yan, J. Wu, B. Zhu, Y. Chen, and X. Chen, "On-chip erbium-doped lithium niobate microcavity laser," Sci. Chin. Phys. Mech. **64**, 234262 (2021).
6. D. G. Grier, "A revolution in optical manipulation," Nature **424**, 810 (2003).
7. M. Padgett and R. Bowman, "Tweezers with a twist," Nat. Photon. **5**, 343 (2011).
8. Z. Shen, L. Su, X. C. Yuan, and Y. C. Shen, "Trapping and rotating of a metallic particle trimer with optical vortex," Appl. Phys. Lett. **109**, 241901 (2016).
9. A. Nicolas, L. Veissier, L. Giner, E. Giacobino, D. Maxein, and J. Laurat, "A quantum memory for orbital angular momentum photonic qubits," Nat. Photon. **8**, 234 (2014).
10. F. Severin, J. Alexander, B. Stefan, and R. M. Monika, "Spiral phase contrast imaging in microscopy," Opt. Express **13**, 689 (2005).
11. S. S. R. Oemrawsingh, J. A. W. van Houwelingen, E. R. Eliel, J. P. Woerdman, E. J. K. Verstegen, J. G. Kloosterboer, and G. W. Hooft, "Production and characterization of spiral phase plates for optical wavelengths," Appl. Opt. **43**, 688 (2004).
12. N. R. Heckenberg, R. McDuff, C. P. Smith, and A. G. White, "Generation of optical phase singularities by computer-generated holograms," Opt. Lett. **17**, 221 (1992).
13. Y. Pan, X. Gao, R. Ma, C. Tu, Y. Li, and H. Wang, "Tunable azimuthally non-uniform orbital angular momentum carried by vector optical fields," Chin. Opt. Lett. **18**, 122601 (2020).
14. B. Y. Wei, S. Liu, P. Chen, S. X. Qi, Y. Zhang, W. Hu, Y. Q. Lu, and J. L. Zhao, "Vortex Airy beams directly generated via liquid crystal q-Airy-plates," Appl. Phys. Lett. **112**, 121101 (2018).
15. X. Cai, J. Wang, M. J. Strain, B. Johnson-Morris, J. Zhu, M. Sorel, J. L. O'Brien, M. G. Thompson, and S. Yu, "Integrated compact optical vortex beam emitters," Science **338**, 363 (2012).
16. B. Etienne, M. Naoki, M. Hiroaki, and J. Saulius, "Optical vortices from liquid crystal droplets," Phys. Rev. Lett. **103**, 103903 (2009).
17. H. Li, H. Liu, and X. Chen, "Nonlinear generation of Airy vortex beam," Opt. Express **26**, 21204 (2018).
18. B. Alon and A. Ady, "Generation of optical vortex beams by nonlinear wave mixing," Opt. Express **15**, 17619 (2007).
19. C. Lin, Y. Chen, X. Li, L. Yang, R. Ni, G. Zhao, Y. Zhang, X. Hu, and S. Zhu, "Frequency-doubled vortex beam emitter based on nonlinear Cherenkov radiation," Chin. Opt. Lett. **18**, 071902 (2020).
20. Y. Wu, R. Ni, Z. Xu, Y. Wu, X. Fang, D. Wei, X. Hu, Y. Zhang, M. Xiao, and S. Zhu, "Tunable third harmonic generation of vortex beams in an optical superlattice," Opt. Express **25**, 30820 (2017).
21. F. Kong, C. Zhang, F. Bouchard, Z. Li, G. G. Brown, H. K. Dong, T. J. Hammond, L. Arissian, R. W. Boyd, and E. Karimi, "Controlling the orbital angular momentum of high harmonic vortices," Nat. Commun. **8**, 14970 (2017).
22. G. Genevieve, L. Jonathan, K. T. Kim, T. J. Hammond, E. Frumker, R. W. Boyd, and P. B. Corkum, "Creating high-harmonic beams with controlled orbital angular momentum," Phys. Rev. Lett. **113**, 153901 (2014).
23. D. Gauthier, P. R. Ribič, G. Adhikary, A. Camper, C. Chappuis, R. Cucini, L. F. Dimauro, G. Dovillaire, F. Frassetto, and R. Géneaux, "Tunable orbital angular momentum in high-harmonic generation," Nat. Commun. **8**, 14971 (2017).
24. H. Jiang, X. Yan, H. Liang, R. Luo, X. Chen, Y. Chen, and Q. Lin, "High harmonic optomechanical oscillations in the lithium niobate photonic crystal nanocavity," Appl. Phys. Lett. **117**, 081102 (2020).
25. H. Li, H. Liu, and X. Chen, "Nonlinear vortex beam array generation by spatially modulated fundamental wave," Opt. Express **25**, 28668 (2017).
26. H. Zhou, H. Liu, M. Sang, J. Li, and X. Chen, "Nonlinear Raman–Nath second harmonic generation of hybrid structured fundamental wave," Opt. Express **25**, 3774 (2017).
27. H. Liu, J. Li, X. Zhao, Y. Zheng, and X. Chen, "Nonlinear Raman–Nath second harmonic generation with structured fundamental wave," Opt. Express **24**, 3774 (2016).
28. G. H. Kim, H. J. Lee, J. U. Kim, and H. Suk, "Propagation dynamics of optical vortices with anisotropic phase profiles," J. Opt. Soc. Am. B **20**, 351 (2003).